Available online at www.sciencedirect.com

ScienceDirect

Proceedings of the Combustion Institute 36 (2017) 4313–4320

Proceedings of the Combustion Institute

www.elsevier.com/locate/proci

A comparative experimental and numerical investigation of the heterogeneous and homogeneous combustion characteristics of fuel-rich methane mixtures over rhodium and platinum

Ran Sui, John Mantzaras*, Rolf Bombach

Paul Scherrer Institute, Laboratory of Thermal Processes and Combustion, CH-5232 Villigen PSI, Switzerland

Received 1 December 2015; accepted 1 June 2016
Available online 16 June 2016

Abstract

The heterogeneous and homogeneous combustion of fuel-rich $CH_4/O_2/N_2/CO_2$ mixtures (equivalence ratios $\varphi = 1.8$–3.5) was investigated experimentally and numerically at 5 bar. Experiments were carried out in an optically accessible channel-flow reactor, which was coated with either rhodium or platinum, and involved in situ spatially-resolved Raman measurements of major gas-phase species concentrations for the evaluation of the heterogeneous processes and planar laser induced fluorescence (LIF) of formaldehyde for the assessment of homogeneous combustion. Simulations were performed with an elliptic 2-D code that included detailed heterogeneous and homogeneous chemical reaction mechanisms. The surface reaction mechanism for Rh modestly overpredicted the formation of partial oxidation products (H_2/CO) and underpredicted the total oxidation products (H_2O/CO_2) at $\varphi \geq 3.0$. Rhodium was shown superior to platinum in syngas production and, furthermore, it maintained a good catalytic partial oxidation (CPO) capacity even at the low $\varphi = 1.8$ where Pt showed minimal H_2/CO yields. The higher syngas production in Rh, and in particular of the highly reactive hydrogen, had a drastic impact on the ensuing gas-phase combustion characteristics. While vigorous homogeneous combustion was always established in Rh, it was altogether suppressed in Pt despite the higher attained surface temperatures in Pt. The agreement between LIF-measured and predicted flame anchoring positions and flame lengths in Rh was particularly good. The strong gaseous combustion in Rh had profound implications, as it considerably reduced the length of the oxidation zone in CPO reactors such that the reforming zone could be initiated farther upstream. It was also shown that homogeneous combustion did not affect the reactor thermal management and that it promoted the syngas yields at the reactor outlet.

Keywords: Catalytic partial oxidation of methane on rhodium and platinum; Raman measurements; Planar laser induced fluorescence of formaldehyde; Homogeneous ignition in catalytic partial oxidation; Syngas production

* Corresponding author. Fax: +41 56 3102199.
E-mail address: ioannis.mantzaras@psi.ch
(J. Mantzaras).

http://dx.doi.org/10.1016/j.proci.2016.06.001
1540-7489

1. Introduction

The catalytic partial oxidation (CPO) of methane to syngas is of key importance for the conversion of natural gas and biogas to synthetic liquid fuels and hydrogen. Nickel-based catalysts are cost effective, but they are inferior to noble metals in coking, sulphur, and sintering/deactivation resistance. Rhodium and platinum are intensively investigated, the former due to its higher efficiency towards syngas production and the latter due to its higher tolerance to sulphur poisoning. Mixed catalysts, produced via partial substitution of Pt by Rh or via inclusion of Pt or Rh promoters in Ni, have also been developed for enhanced CPO performance [1,2]. CPO of methane can be accomplished autothermally and selectively in short contact times over Pt-based or Rh-based catalysts [3,4], thus rendering the process particularly attractive for on-board fuel reforming in microreactors, fuel-cells, and also for natural-gas-fueled turbines in power generation [5].

Understanding of the controlling physicochemical processes in methane CPO over Pt and Rh, such as light-off temperatures, syngas yields and selectivities, and extinction characteristics has been aided by recent spatially-resolved 1-D (axial) measurements of temperature and species compositions in honeycomb reactors by means of a traversable thermocouple/capillary-sampling assembly [6–9]. Spatially-resolved 2-D (in both axial and transverse directions) profiles of major gas-phase species concentrations, by means of non-intrusive Raman measurements across the boundary layer of a 7-mm-height Rh/ZrO_2-coated channel, were also reported in the CPO of methane with O_2/N_2 [10] or with $O_2/H_2O/CO_2/N_2$ [11]. Such 2-D measurements are essential for unambiguously identifying potential transport limitations. The aforementioned experiments have led to the development of detailed surface chemical reaction mechanisms for methane CPO over Pt and Rh [3,12,4,13]. Elevated pressures are of interest in gas-to-liquid conversion (whereby the pressure is ideally dictated by the downstream chemical process, e.g. methanol and Fischer-Tropsch synthesis) and also in CPO of natural gas in power generation [14,11].

The present work investigates experimentally and numerically the CPO of methane over Pt and Rh at 5 bar. Experiments were performed in an optically accessible channel-flow reactor. The catalytic processes were assessed with Raman measurements of major gaseous species concentrations and the onset of homogeneous ignition was monitored with planar laser induced fluorescence (LIF) of formaldehyde. Main objectives were to compare the two catalysts in their partial oxidation capacity and particularly in their ability to promote homogeneous combustion.

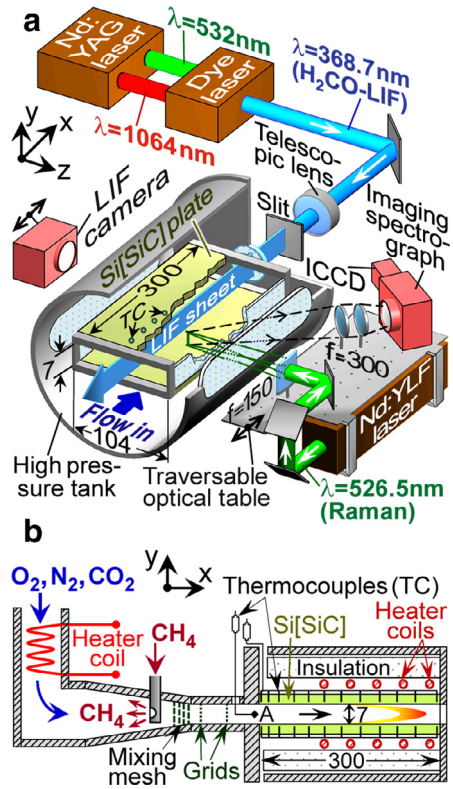

Fig. 1. (a) Test-rig with Raman/LIF setup, (b) reactor details (distances in mm).

2. Experimental

2.1. Catalytic reactor

The reactor comprised two horizontal Si[SiC] ceramic plates (300 mm long (-x), 104 mm wide (-z), 9 mm thick, positioned 7 mm apart (-y)) and two 3-mm-thick vertical quartz windows (see Fig. 1 and [15,16]). The inner Si [SiC] surfaces were covered with Pt or Rh using an identical coating procedure. Plasma vapor deposition (PVD) was employed to first deposit a 1.5-μm-thick non-porous Al_2O_3 layer on Si[SiC] and then a 2.2-μm-thick Pt or Rh layer. The Al_2O_3 layer mitigated chemical interactions between the noble metals and Si [17]. The 2.2-μm-thick noble metal layer closely resembled a polycrystalline Pt or Rh surface and this was verified with total and active surface area measurements using BET (Kr-physisorption) and CO-chemisorption, respectively, which confirmed the lack of surface porosity. Moreover, the presence of noble metal only and the absence of bulk Al or Si at the surface was attested with post-combustion XPS measurements [17].

Surface temperatures were measured by 12 (for each plate) S-type thermocouples positioned along

the x-y symmetry plane (see Fig. 1) and embedded 0.9 mm beneath the catalytic surfaces, through 8.1-mm-deep holes eroded from the rear Si[SiC] surfaces. Over the length $100 < x < 300$ mm, two resistive heater coils with adjustable power were positioned above the Si[SiC] plates to counteract the external heat losses and to control the surface temperatures (Fig. 1b). The reactor assembly was mounted inside a high-pressure cylindrical steel tank. Two 350-mm-long, 50-mm-high and 35-mm-thick quartz windows on the tank allowed for side optical access (Fig. 1a). Two additional quartz windows at the rear tank flange and the reactor exhaust facilitated streamwise optical access for the H_2CO-LIF laser beam.

Pressurized bottles supplied CH_4, O_2, N_2 (and CO_2 when needed to control homogeneous ignition) with the flowrates controlled by four Brooks mass flowmeters. The $O_2/N_2/CO_2$ gases were mixed in two static mixers and preheated by an electric heater. Methane was injected counterflow to the preheated $O_2/N_2/CO_2$ stream (Fig. 1b) inside a 200-mm-long conical mixing section (especially designed to avoid autoignition of the very reactive gaseous mixture), by means of eight 0.5-mm-diameter nozzles arranged laterally (z-direction). The conical section allowed for a gradual transition of the flow cross-section from circular (35-mm-diameter) to rectangular (104×7 mm^2). A 3-mm-thick wire mesh and two grids (0.5 mm^2 open area) inside this section yielded a uniform flow and good mixing of methane with $O_2/N_2/CO_2$. Optimization of the mesh/grids positions was accomplished with the following measurements, performed at the exit plane of the stand-alone conical section: hot wire velocimetry to assess the flow uniformity, and planar LIF of NO (doped into the CH_4 stream, excitation at 226.25 nm, detection at 240–265 nm) to assess the mixing quality. The gas inlet temperature at the reactor entry ($x=0$, position A in Fig. 1b) was monitored by a K-type thermocouple, which was radiation-shielded by placing it inside a 1.2-mm-ID and 2.0-mm-OD ceramic tube.

2.2. Laser diagnostics

Figure 1a depicts the planar-LIF and Raman setups. The diminishing OH levels at fuel-rich stoichiometries precluded planar OH-LIF [11], such that H_2CO-LIF was adopted. The second harmonic of an Nd:YAG laser (Quantel YG781C20-CL-D-LNE3, pulse duration 10 ns and repetition rate 20 Hz) pumped an Rh6G dye laser (Quantel TDL90-NBP2EWT-UVT3). The remaining 1064 nm fundamental Nd:YAG radiation was additively frequency-mixed with the dye-laser output to produce the H_2CO excitation. The resulting 368.7 nm beam (~12 mJ/pulse) excited transitions in the vicinity of the ^{R}R (A-X) 4^0_1 hot band, ensuring a strong signal at elevated temperatures. A system of telescopic lenses and a slit converted the UV beam into a vertical light sheet that propagated counterflow along the x-y symmetry plane (Fig. 1a). The comparatively wide light sheet along with the high intrinsic quenching and low oscillator strength of carbonyl compounds excluded saturation of the fluorescence signal.

An intensified CCD camera (LaVision Imager Compact HiRes-IRO, 1392×1024 pixels binned to 696×512) recorded the fluorescence emission at 90° through the reactor and tank side-windows. Fluorescence was collected from a narrow wavelength range (426.5–433.5 nm) of the H_2CO emission (400–550 nm), using a BK-430-7 interference filter in front of an f100mm/2.8 lens, thus minimizing interferences from fluorescence signals of other species. Channel areas 100×7 mm^2 were recorded on 1360×70 pixels of the CCD. To map the entire reactor, the camera was traversed axially in 50 mm steps. Given the steady operating conditions, at each position 960 images were averaged to increase the signal-to-noise ratio.

For the Raman measurements a frequency-doubled pulsed Nd:YLF laser at 526.5 nm (Quantronix Darwin-Duo, 2 kHz repetition frequency) was used (Fig. 1a) with a pulse duration and energy of 120 ns and 30 mJ, respectively. An $f=150$ mm cylindrical lens focused the laser beam into a ~0.3-mm-thick vertical line, which spanned the entire 7 mm channel-height and was offset laterally (-z) 15 mm from the x-y symmetry plane to increase the collection angle and minimize thermal beam steering, as in earlier studies [15,18]. Two $f=300$ mm lenses focused the Raman-scattered light into the entrance slit of a 25 cm spectrograph (Chromex-250i) equipped with an intensified CCD camera (Princeton Instruments PI-MAX1024GIII, 640×255 pixels corresponding to spectral shift and y-distance, respectively). The 7 mm channel-height was resolved with 220 pixels, which were binned to 64 pixels.

Excitation radiation was suppressed by an appropriately tilted Kaiser-Optical-Systems 532 nm holographic notch filter and an OG550 Schott glass filter. The Nd:YLF laser, the sending/collecting optics and the spectrograph were mounted on a traversable optical table (Fig. 1a), allowing Raman measurements over $9 \le x \le 126$ mm. Scattered light from 360,000 laser pulses was integrated on the detector chip to increase the signal-to-noise ratio. The measurement accuracy was $\pm3\%$ for species concentrations $\ge 3\%$ vol. and $\pm8\%$ for concentrations as low as 0.5% vol., while lower contents could not be accurately resolved. Data closer than 0.7 mm to the catalytic walls were discarded due to low signal-to-noise ratios.

Table. 1
Experimental conditions.[a]

Case	φ	U_{IN}	T_{IN}	CH_4	O_2	CO_2
1	1.8	0.47	429 (426)	17.3	19.0	–
2	2.3	0.28	457 (476)	23.0	20.0	15.0
3	3.0	0.28	439 (440)	25.9	17.4	–
4	3.0	0.36	453 (463)	25.5	17.0	15.1
5*	3.5	0.57	453	28.3	16.1	14.8

[a] Equivalence ratio, inlet velocity (m/s), inlet temperature (K)(first entry Rh, second Pt), inlet vol. content (%) with balance N_2.
* Only with rhodium.

3. Numerical

A steady elliptic 2-D CFD code was used (details in [15,16]). A staggered grid with 440×60 points (in -x and -y, respectively) for the 300×7 mm^2 domain was sufficient to produce a grid-independent solution. The temperature, axial velocity, and species mass fractions were uniform at the inlet. Temperature profiles at the lower ($y=0$) and upper ($y=7$ mm) walls were prescribed by fitting curves through the 12 thermocouple measurements on each Si[SiC] plate.

For Rh the detailed mechanism by Schwiedernoch et al. [19] was used (38 reactions, 12 surface and 6 gaseous species), which was tuned against methane-CPO measurements in a honeycomb reactor. For Pt the detailed mechanism by Quiceno et al. [12] was employed (34 reactions, 11 surface species, 6 gaseous species), which has been tested against methane-CPO in platinum wire gauzes. Gas-phase chemistry was described by the elementary C_2/H/O mechanism of Warnatz et al. [20] (164 reversible reactions, 34 species). This mechanism has reproduced homogeneous ignition characteristics in CPO of methane with O_2/ H_2O/CO_2/N_2 over a technical Rh/ZrO_2 catalyst [11].

Surface and gas-phase reaction rates were evaluated with Surface-Chemkin [21] and Chemkin [22], respectively. Mixture-average diffusion including thermal diffusion for H_2 was used, along with the Chemkin transport database [23].

4. Results and discussion

The experiments encompassed equivalence ratios $\varphi=1.8$–3.5 at 5 bar (see Table. 1). Cases 1–4 referred to both Rh and Pt, while Case 5 only to Rh. Common operating conditions were adopted for the Rh and Pt Cases 1–4, including the same power of the Si[SiC] heater coils. The inlet temperatures, however, differed on Rh and Pt by 1–19 K (see Table. 1) since the in-channel processes were different and this altered the heat conducted upstream into the mixing section. All flows were laminar with inlet Reynolds numbers 310–670 (based on the 7-mm-height and the inlet velocities U_{IN} in Table. 1 that referred to the 5 bar pressure and the measured T_{IN}).

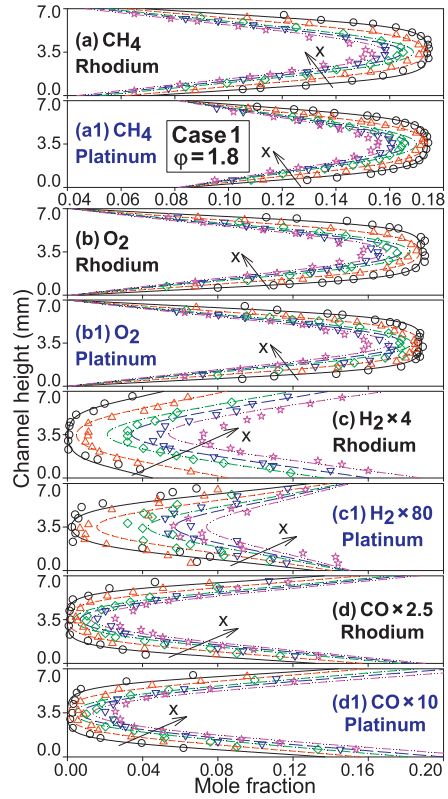

Fig. 2. Transverse profiles of species mole fractions (lines: predictions, symbols: Raman measurements) for Case 1, Rh (a-d) and Pt (a1-d1): x = 9 mm (solid lines, circles), 21 mm (short dashed lines, upper-triangles), 41 mm (dashed-dotted lines, diamonds), 51 mm (long dashed lines, lower-triangles), and 66 mm (dashed-double-dotted lines, stars).

4.1. Comparisons of Raman measurements and predictions

The catalytic processes were studied by comparing Raman-measured and predicted transverse profiles of major gas-phase species mole fractions. Comparisons are shown in Fig. 2 (Case 1, $\varphi=1.8$) and Fig. 3 (Case 3, $\varphi=3.0$) for both catalysts, at five streamwise locations down to $x=66$ mm. The extent $x \leq 66$ mm pertained to the oxidation zone of CPO [10,6], wherein oxygen was not fully depleted. Moreover, all profiles in Figs. 2 and 3 were upstream of the homogeneous ignition locations, so as to avoid falsification of the catalytic processes by gaseous chemistry (homogeneous combustion will be elaborated in Section 4.3). In Fig. 2 the reactants CH_4/O_2 and partial oxidation products H_2/CO are plotted, while in Fig. 3 CH_4/O_2/H_2/H_2O are shown (H_2O only for Rh). Measured upper and lower wall

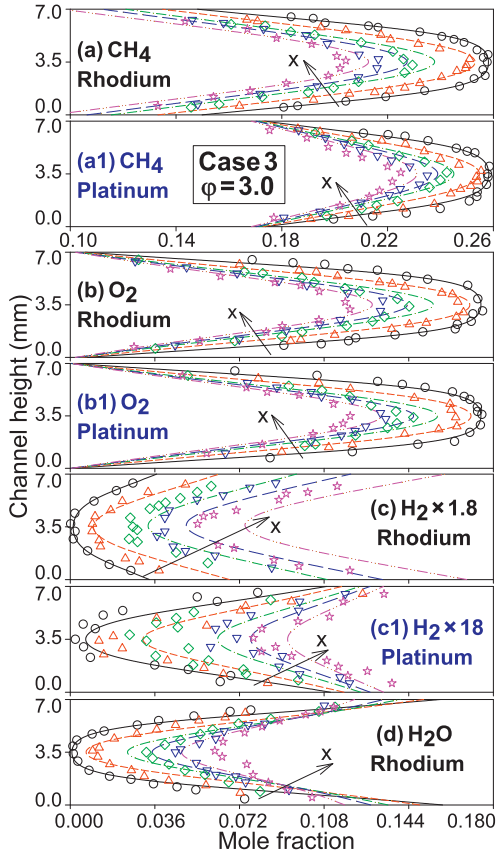

Fig. 3. Transverse profiles of species mole fractions (lines: predictions, symbols: Raman measurements) for Case 3, Rh (a-d) and Pt (a1-c1). Notation of x-positions as in Fig. 2.

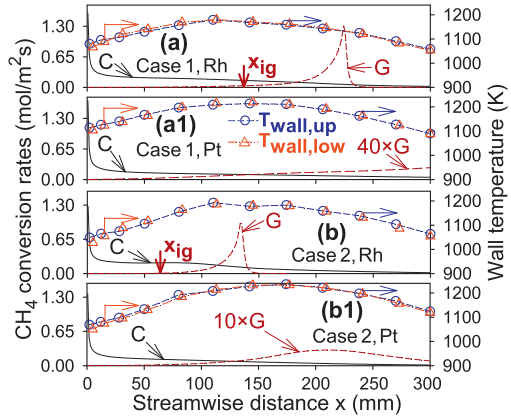

Fig. 4. Predicted streamwise profiles of catalytic (C) and gaseous (G) methane conversion rates for Cases 1 and 2, Rh (a-b) and Pt (a1-b1), and measured wall temperatures. Vertical arrows denote the homogeneous ignition locations (x_{ig}) for Rh.

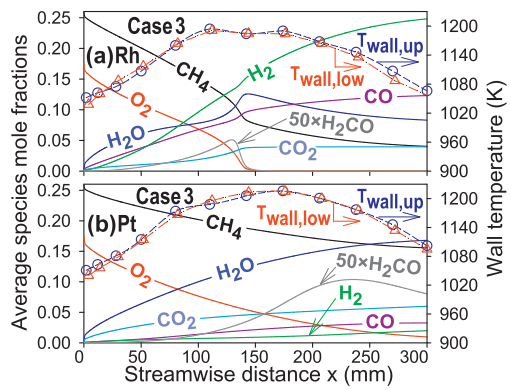

Fig. 5. Predicted streamwise profiles of transversely-averaged species mole fractions for Case 3, (a) Rh, (b) Pt, and measured wall temperatures.

temperatures (see Fig. 4 for Cases 1 and 2, and Fig. 5 for Case 3) did not exceed 1208 K on Rh and 1250 K on Pt.

Comparisons at $\varphi = 1.8$ were quite favorable, with the simulations modestly underpredicting the methane conversion for either Rh or Pt (Fig. 2(a, a1)). The deficient O_2 reactant approached transport-limited conversion on both catalysts. This was manifested by the computed low wall-to-center O_2 mole fraction ratios, $X_{O2}(y = 0$ or 7 mm$)/X_{O2}(y = 3.5$ mm), which were less than 2.8% on Rh and less than 1.0% on Pt in Fig. 2(b, b1). This behavior was also supported by the measurements, despite the lack of Raman data within 0.7 mm from the walls. Production of H_2 and CO on Rh was moderately underpredicted. Computed hydrogen mole fractions, X_{H2}, for Rh were up to 0.047 at the wall and 0.014 at the channel center (Fig. 2(c)) with corresponding values for X_{CO} 0.076 and 0.005 ((Fig. 2(d)). The appreciably higher values of H_2 compared to CO at the channel center ($y = 3.5$ mm) were due to the higher molecular diffusivity of H_2.

On the other hand, Pt had a minimal H_2 production (X_{H2} less than 0.002, Fig. 2(c1)); such low levels could not be accurately measured, leading to a larger data scatter.

For the higher $\varphi = 3.0$ in Fig. 3, O_2 conversion was again close to the transport limit for both catalysts. The H_2 production in Rh (Fig. 3(c)) nearly doubled compared to $\varphi = 1.8$ (Fig. 2(c)) while it quadrupled in Pt. Hydrogen production in Rh was somewhat overpredicted at $\varphi = 3.0$ and this was accompanied by an underprediction of H_2O (Fig. 3(d)). Overprediction (underprediction) was also observed for the CO (CO_2) mole fraction (not shown in Fig. 3). The slight overprediction of partial over total oxidation products in Rh with the present kinetic model was also observed earlier [10] for $\varphi > 2.5$. Finally, X_{CH4} was always lower in Rh compared to Pt (Figs. 2(a, a1) and 3(a, a1)).

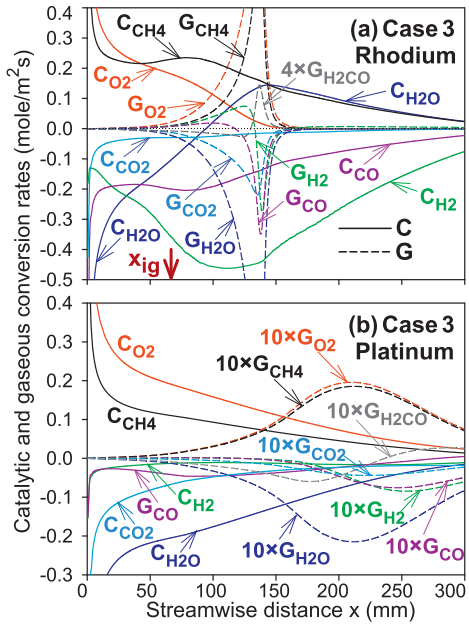

Fig. 6. Predicted catalytic (C) and gaseous (G) species conversion rates, Case 3: (a) Rh, (b) Pt.

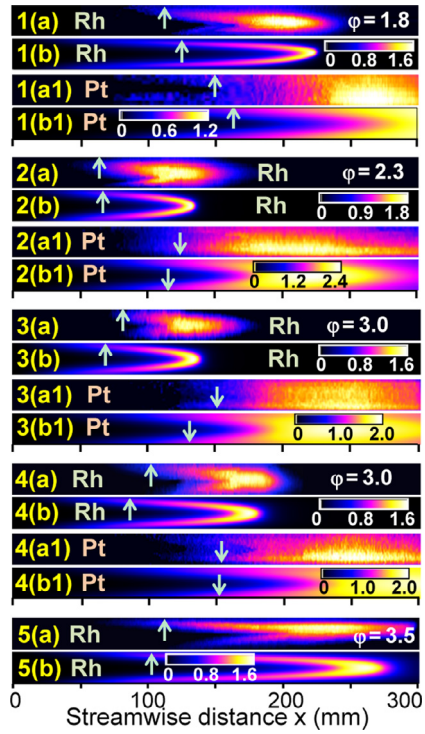

Fig. 7. Formaldehyde distributions, Cases 1-5: (a) H_2CO-LIF in Rh, (a1) H_2CO-LIF in Pt, (b) predictions Rh, (b1) predictions Pt. Color bars give the predicted formaldehyde (1000×ppmv). Vertical arrows indicate locations where formaldehyde reached 5% of its peak value.

This was because Rh consumed more CH_4 with a given amount of O_2 as it produced more partial oxidation products compared to Pt, which in turn formed more total oxidation products.

4.2. Synthesis gas production

The production of syngas over Rh and Pt is further elaborated for Case 3. In Fig. 5 computed transversely-averaged streamwise profiles of species mole fractions are shown, while in Fig. 6 streamwise profiles of the catalytic (C) and gas-phase (G) species conversion rates are plotted (positive rates in Fig. 6 denote species destruction while negative rates denote production). The G rates were computed by integrating the volumetric gaseous rates over the entire 7-mm-height. On the Rh catalyst vigorous homogeneous combustion was initiated, as manifested by the substantial G conversions of all major species in Fig. 6a. Homogeneous ignition (defined herein as the far-upstream position whereby X_{H2CO} reached 5% of its peak value in the channel) was initiated at $x_{ig} = 68$ mm in Rh. However, in Pt (Fig. 6b) there was a minimal contribution of gaseous combustion, as indicated by the very low G rates (for clarity, the G rates have been multiplied by 10).

For Rh and upstream of homogeneous ignition ($x < x_{ig}$), the catalytic molar conversion ratio C_{O2}/C_{CH4} was ~2 at $x < 15$ mm (Fig. 6a) indicating total oxidation of methane. However for 45 mm $< x < x_{ig} = 68$ mm, $C_{O2}/C_{CH4} < 1$ indicating a combination of total and partial oxidation. For Pt in Fig. 6b, the catalytic production of H_2/CO was much weaker and total over partial oxidation was favored, as also attested by the always larger-than-unity C_{O2}/C_{CH4} conversion ratio. The profiles in Fig. 5 indicated that, at the position $x_{ig} = 68$ mm on the Rh-catalyst, the y-averaged mole fractions of H_2 and CO were 0.055 and 0.049, respectively. On the other hand, for the Pt catalyst (Fig. 5b) the H_2 and CO average mole fractions were only 0.0198 and 0.0326 at the outlet ($x = 300$ mm).

Finally, for the three cases in Table. 1 with CO_2 addition, simulations have shown that the impact of dry reforming was minimal. The same was also reported in [6] in methane CPO over Rh and Pt, for similar peak surface temperatures as in the present work.

4.3. Homogeneous combustion

Measured and predicted H_2CO maps are shown in Fig. 7. The H_2CO-LIF signals were strong in both Pt and Rh (the predicted H_2CO had also high levels, see color-coded bars in Fig. 7); however, vigorous homogeneous combustion was established only in Rh. This was manifested by the

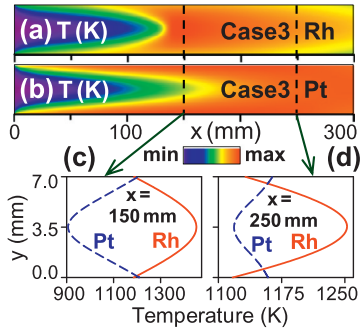

Fig. 8. Predicted temperature maps in Case 3 for (a) Rh and (b) Pt. Temperature levels given in the color bar, minimum: 439 K and maximum: 1460 K (Rh) or 1210 K (Pt). Transverse profiles of temperature for Rh and Pt at (c) x = 150 and (d) x = 250 mm.

vanishing H_2CO in the post-flame zones of all Rh cases. H_2CO was produced homogeneously in the gaseous induction zone and was then fully consumed in the flame (see G_{H2CO} in Fig. 6a and the y-averaged X_{H2CO} in Fig. 5a). However, H_2CO in Pt was produced homogeneously at $x < 235$ mm and then consumed at $x > 235$ mm (Fig. 6b). Due to the lack of vigorous homogeneous combustion in Pt, the H_2CO consumption rate was low, such that copious amounts of H_2CO remained at the channel exit. The contribution of gaseous chemistry to the production/destruction of major species in Pt was minimal, as seen in Fig. 6b. Additionally, the predicted gas-phase exothermicity in Rh was significant (peak gas temperatures 270 K higher than the wall temperatures), while in Pt there was no appreciable gaseous heat release. This is illustrated in Fig. 8, providing predicted 2-D temperature distributions for both Rh and Pt in Case 3 as well as transverse temperature profiles at two selected streamwise positions.

The agreement between measurements and predictions in Rh was quite good for the flame lengths and homogeneous ignition positions x_{ig} (far-upstream locations where H_2CO rose to 5% of its peak measured or predicted value). This definition of x_{ig} in Rh closely corresponded to the rise in G conversions of all major species (see Figs. 6a and 4(a, b), where x_{ig} are marked). There were nonetheless differences in the spatial distribution of formaldehyde in Rh. The predicted formaldehyde was concentrated in thin reaction zones, whereas the measurements indicated a broader distribution in the pre-flame region. This was also observed in [11] and was attributed [24] to the exaggerated signal contribution of the colder, higher-density zones upstream of the flame. For Pt, the agreement between measurements and predictions was also good in terms of H_2CO distributions and locations of 5% H_2CO rise (albeit these positions did not correspond to the onset of vigorous gaseous combustion).

Rhodium promoted homogeneous combustion despite two counteracting effects: a) the surface temperatures were always lower in Rh compared to Pt (by up to 60 K, see Fig. 4) since Pt favored total over partial oxidation, and b) the methane catalytic conversion was always higher in Rh than in Pt (as discussed in Section 4.1) and hence less fuel was available for the gaseous pathway. Homogeneous combustion was favored in Rh due to its enhanced syngas production, especially H_2. This was confirmed with sensitivity analysis in a Surface Perfectly Stirred Reactor (SPSR) [25]; the most sensitive catalytic reactions affecting the reactor temperature were, apart from the CH_4 and O_2 adsorption/desorption, those reactions impacting hydrogen production: H_2 adsorption/desorption, $H_2+2Rh(s) \Leftrightarrow 2H(s)$, and reactions that depleted H(s) and hence reduced the amount of desorbed hydrogen ($H(s)+O(s) \rightarrow OH(s)+Rh(s)$, $H(s)+OH(s) \rightarrow H_2O(s)+Rh(s)$).

The onset of homogeneous combustion in Rh shortened considerably the CPO oxidation zone, as seen in Fig. 5a where O_2 was fully consumed at $x \approx 148$ mm (by re-computing this case without gas-phase chemistry, the oxidation zone extended to the outlet, $x = 300$ mm, with corresponding $X_{O2} = 0.013$). Downstream of the oxidation zone in Fig. 6a ($x > 148$ mm), catalytic steam reforming was dominant ($CH_4+H_2O \rightarrow CO+3H_2$) as manifested by the ratios $C_{CH4}/C_{H2O} \sim 1$ and $C_{H2}/C_{CO} \sim 3$. On the other hand, gas-phase steam reforming was minimal as seen from the G_{CH4} and G_{H2O} profiles in Fig. 6a, at $x > 148$ mm. Gaseous combustion in Rh was beneficial in reducing the oxidation zone length and, moreover, it promoted the H_2 and CO yields at the reactor exit. For example, simulations for Case 3 in Rh without gaseous chemistry yielded $X_{H2} = 0.213$ at $x = 300$ mm, while the hetero-/homogeneous simulations in Fig. 5a resulted in $X_{H2} = 0.248$. Moreover, gas-phase combustion did not pose thermal management concerns, since the peak flame temperatures were concentrated in the channel core, away from the channel walls as shown in Fig. 8(c, d) for Rh. As discussed in [26] this was a general property of hetero-/homogeneous combustion with deficient reactants having Lewis numbers larger than unity (the deficient O_2 had Lewis numbers 1.05–1.14 for the cases in Table. 1). Finally, gaseous combustion did not appear to affect the low propensity of Rh for coking and no carbon deposition was observed on the catalyst or the exhaust section. For Pt, even in the absence of gaseous combustion, coking was initially observed at $\varphi = 3.5$.

5. Conclusions

The hetero-/homogeneous combustion of fuel-rich $CH_4/O_2/N_2/CO_2$ mixtures was investigated over Rh and Pt at 5 bar. In situ Raman

measurements of major gas-phase species concentrations and 2-D simulations showed that the reaction mechanism for methane-CPO on Rh modestly underpredicted (overpredicted) the H_2/CO yields at $\varphi = 1.8$ ($\varphi \geq 3.0$). Rhodium was superior to Pt in syngas production and, moreover, it maintained its CPO capacity even at a low $\varphi = 1.8$ wherein Pt showed minimal H_2/CO yields. The higher H_2 production of Rh had a profound impact on gaseous combustion. While vigorous homogeneous combustion was attained in Rh, it was altogether suppressed in Pt. The presence of gaseous combustion in Rh substantially reduced the oxidation zone length, such that the reforming action could be initiated farther upstream. Finally, homogeneous combustion promoted the syngas yields at the reactor outlet and did not affect the reactor thermal management since the peak temperatures were attained in the gas and not on the catalytic walls.

Acknowledgments

Support was provided by the EU project HRC-Power. We thank Mr. Jürgen Theile for aiding the measurements.

References

[1] S. Cimino, L. Lisi, G. Russo, R. Torbati, *Catal. Today* 154 (2010) 283–292.
[2] B.C. Enger, R. Lodeng, A. Holmen, *Catal. Lett.* 134 (2010) 13–23.
[3] O. Deutschmann, L.D. Schmidt, *AIChE* 44 (1998) 2465–2477.
[4] M. Maestri, D.G. Vlachos, A. Beretta, P. Forzatti, G. Groppi, E. Tronconi, *Top. Catal.* 52 (2009) 1983–1988.
[5] S. Eriksson, M. Wolf, A. Schneider, J. Mantzaras, F. Raimondi, M. Boutonnet, et al., *Catal. Today* 117 (2006) 447–453.
[6] R. Horn, K.A. Williams, N.J. Degenstein, A. Bitsch-Larsen, D.D. Nogare, S.A. Tupy, et al., *J. Catal.* 249 (2007) 380–393.
[7] A. Donazzi, M. Maestri, B.C. Michael, A. Beretta, P. Forzatti, G. Groppi, et al., *J. Catal.* 275 (2010) 270–279.
[8] C. Diehm, O. Deutschmann, *Int. J. Hydrog. Energy* 39 (2014) 17998–18004.
[9] A. Donazzi, D. Livio, C. Diehm, A. Beretta, G. Groppi, P. Forzatti, *Appl. Catal. A-Gen.* 469 (2014) 52–64.
[10] C. Appel, J. Mantzaras, R. Schaeren, R. Bombach, A. Inauen, N. Tylli, et al., in: Proc. Combust. Inst., 30, 2005, pp. 2509–2517.
[11] A. Schneider, J. Mantzaras, R. Bombach, S. Schenker, N. Tylli, P. Jansohn, in: Proc. Combust. Inst., 31, 2007, pp. 1973–1981.
[12] R. Quiceno, J. Perez-Ramirez, J. Warnatz, O. Deutschmann, *Appl. Catal. A-Gen.* 303 (2006) 166–176.
[13] M. Maestri, D.G. Vlachos, A. Beretta, G. Groppi, E. Rronconi, *AIChE J.* 55 (2009) 993–1008.
[14] S. Eriksson, A. Schneider, J. Mantzaras, M. Wolf, S. Jaras, *Chem. Eng. Sci.* 62 (2007) 3991–4011.
[15] Y. Ghermay, J. Mantzaras, R. Bombach, K. Boulouchos, *Combust. Flame* 158 (2011) 1491–1506.
[16] X. Zheng, J. Mantzaras, R. Bombach, *Combust. Flame* 161 (2014) 332–346.
[17] M. Reinke, J. Mantzaras, R. Schaeren, R. Bombach, A. Inauen, S. Schenker, *Combust. Flame* 136 (2004) 217–240.
[18] M. Schultze, J. Mantzaras, F. Grygier, R. Bombach, in: Proc. Combust. Inst., 35, 2015, pp. 2223–2231.
[19] R. Schwiedernoch, S. Tischer, C. Correa, O. Deutschmann, *Chem. Eng. Sci.* 58 (2003) 633–642.
[20] J. Warnatz, R.W. Dibble, U. Maas, Combustion, Physical and Chemical Fundamentals, Modeling and Simulation, Springer-Verlag, New York, 1996, p. 69.
[21] M.E. Coltrin, R.J. Kee, F.M. Rupley, Surface Chemkin: *A Fortran package for analyzing heterogeneous chemical kinetics at the solid surface-gas phase interface*, Report No. SAND90-8003C, Sandia National Laboratories, 1996.
[22] R.J. Kee, F.M. Rupley, J.A. Miller, Chemkin II: *A Fortran chemical kinetics package for the analysis of gas-phase chemical kinetics*, Report No. SAND89-8009B, Sandia National Laboratories, 1996.
[23] R.J. Kee, G. Dixon-Lewis, J. Warnatz, M.E. Coltrin, J.A. Miller, *A Fortran computer code package for the evaluation of gas-phase multicomponent transport properties*, Report No. SAND86-8246, Sandia National Laboratories, 1996.
[24] D.I. Shin, T. Dreier, J. Wolfrum, *Appl. Phys. B-Lasers Opt.* 72 (2001) 257–261.
[25] H.K. Moffat, R.J. Kee, J.F. Grcar, J.A. Miller, Surface PSR: *A Fortran program for modeling well-stirred reactors with gas and surface reactions*, Report No. SAND91-8001, Sandia National Laboratories, 1993.
[26] X. Zheng, J. Mantzaras, *Combust. Flame* 161 (2014) 1911–1922.